Experimental Thermal and Fluid Science 38 (2012) 115–126

Contents lists available at SciVerse ScienceDirect

Experimental Thermal and Fluid Science

journal homepage: www.elsevier.com/locate/etfs

PIV studies around a bus model

Cahit Gurlek [a], Besir Sahin [b,*], Gokturk Memduh Ozkan [b]

[a] Cumhuriyet University, Faculty of Engineering, Mechanical Engineering Department, 58140 Sivas, Turkey
[b] Cukurova University, Faculty of Engineering and Architecture, Mechanical Engineering Department, 01330 Adana, Turkey

ARTICLE INFO

Article history:
Received 7 April 2010
Received in revised form 23 July 2011
Accepted 30 November 2011
Available online 9 December 2011

Keywords:
Ground vehicle aerodynamics
PIV
Rectangular body
Wake flow

ABSTRACT

The three-dimensional flow structures around a bus model have been investigated experimentally. The time-averaged and instantaneous velocity vector maps, vorticity contours, streamline topology and other turbulent quantities were obtained using the particle image velocimetry (PIV) technique. The measurements were carried out in vertical, horizontal and cross-sectional planes. The three-dimensional wake region was asymmetric in the vertical plane while the wake flow was almost symmetric in the horizontal plane. In cross-planes the flow field downstream of the model is dominated by a pair of counter rotating vortices originating from the bottom and upper corners of the model.

1. Introduction

Land transportation is the most widely used passenger and freight transportation in Turkey and 95% of total of passenger transport performed by road. It is known that a 10% drag reduction leads to approximately a 5% reduction of the fuel consumption of a bus at a common highway speed [1]. An estimated total savings of $100 million per year can be recognized in Turkey alone for just a 5% reduction in fuel use in intercity passenger transportation by buses.

Vehicle aerodynamics has become more important due to fuel prices and environmental pollutions in recent years. Due to these reasons, aerodynamics of ground vehicles has been studied experimentally and numerically by many researchers. Most previous studies have used simplified vehicle models that can generate similar features of the flow around real vehicles [2–6]. The best known simplified vehicle is the Ahmed body, following the study by Ahmed et al. [2]. The flow field in the wake region is characterized by a pair of horseshoe vortices (situated one above the other) and trailing vortices emanating from the slant side edges. Duell and George [3] presented results of flow measurements in the near wake of a bus-shaped ground vehicle based on the Ahmed body. They measured vortex shedding at a dimensionless frequency and Strouhal number $St = 1.157$ at the beginning of the shear layer where the model boundary layer separates from the body. Vortex pairing was observed close to the free stagnation point, resulting in the halving of the characteristic frequency. The periodic pumping caused interaction of the upper and lower portions of the ring vortex at $St = 0.069$, resulting in periodic base pressure fluctuations. Spohn and Gillieron [4] studied the complex flow phenomena occurring around the simplified geometry of the road vehicle via a flow visualization water tunnel based technique. They found that the near-wake flow was dominated by a pair of counter-rotating trailing vortices, which was bounded by a central separation bubble that enclosed a flow reversal region. Although the Reynolds number based on the incoming flow velocity and the length of the bluff body was about 3×10^4, it was concluded that the position and topology of the flow structure are in good agreement with the previous studies, and the use of low speed water tunnels appears to be a useful tool to complement wind tunnel studies. The flow structure around a rectangular shaped bus model has been investigated experimentally by Gurlek et al. [7] using PIV measurements and the flow visualization technique. It is reported that a large reverse flow region is observed on the model roof at the vertical symmetry plane. The separated leading edge shear layers reattached approximately at the same locations both on the roof and vertical side walls of the model due to the geometrical similarity. The distance of the reattachment point to the leading edge was $x/H = 1.3$. A shear layer emanating from the top side of the model dominated the wake region downstream of the model with a larger length scale compared to the underbody shear layer. The rates of fluctuations are higher along the upper shear layer due to the high rate of momentum. Drag reduction is one of the main objectives of academic and industrial research. A comprehensive study of aerodynamic drag-reduction devices for ground vehicles can be found in [8].

Flow fields around simplified ground vehicles have been investigated by a large number of numerical studies to validate CFD

* Corresponding author. Tel.: +90 322 3387063; fax: +90 322 3386126.
E-mail address: bsahin@cu.edu.tr (B. Sahin).

0894-1777/$ - see front matter © 2011 Elsevier Inc. All rights reserved.
doi:10.1016/j.expthermflusci.2011.11.014

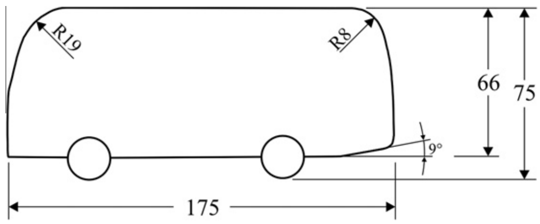

Fig. 1. Schematic of the model.

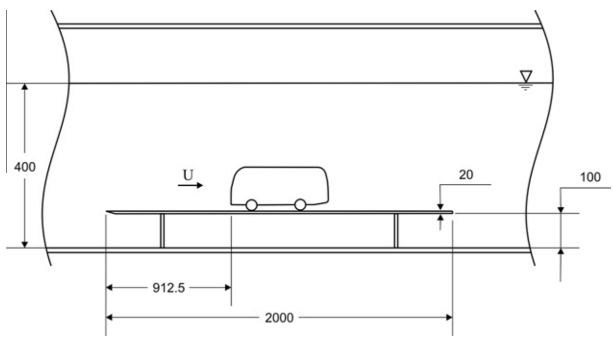

Fig. 2. Location of the model in the water channel (side view).

technique using different turbulent models [9–12]. Krajnovic and Davidson [10] analyzed the flow around a simplified bus model in order to use the large-eddy simulation method (LES). Mechanisms of the formation of flow structures, instantaneous and time-averaged flow features were verified with the previous experimental results. The computed aerodynamic forces and their time history were used to reveal the characteristic frequencies of the flow motion around the body. They also reported that at the Reynolds number of 2.1×10^5 (based on the model height and the incoming flow velocity), the flow produced features and aerodynamic forces relevant for the higher Reynolds numbers.

The main goal of the present research is to visualize the flow structure quantitatively around a bus model using a laser based particle image velocimetry (PIV) technique. The previous studies on wakes generated by bluff-bodies have generally concentrated on studying the frequency of vortex shedding, drag coefficient, base pressure, location of flow separation points, development of the vortex structures and the wake spread rate. The present investigation aims to gain further insight into the vortical flow mechanism that affects instantaneous patterns of vorticity concentrations. Patterns of instantaneous vortices and distributions of velocity vectors of wake flow regions and turbulent statistics are studied to reveal the detailed features of the instantaneous flow structure. It is also aimed at providing an experimental database that can be used as a benchmark to validate CFD simulations.

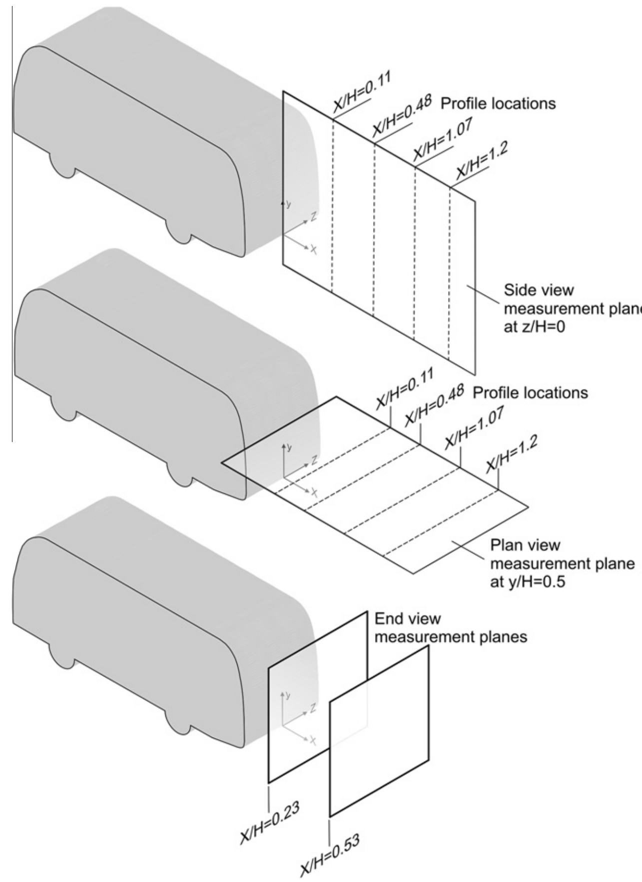

Fig. 3. PIV measurement planes.

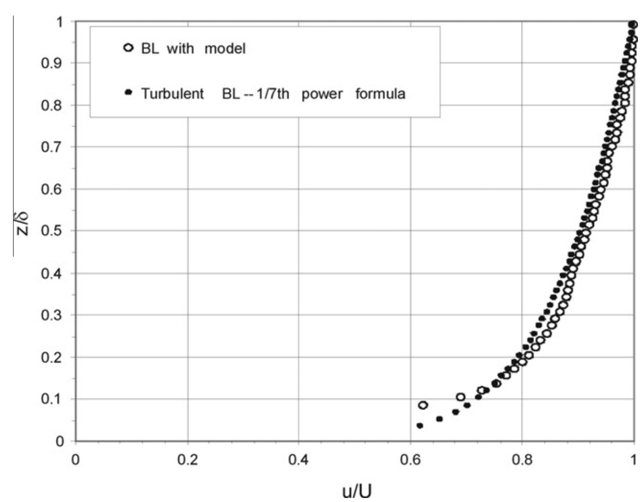

Fig. 4. Boundary layer profile in front of the model.

2. Experimental arrangement

The experiments were performed in a free surface water channel with a working section 1000 mm wide, 750 mm deep, 8000 mm long and a freestream turbulence level of less than 0.5%. The water height was maintained at an elevation of 400 mm. Throughout the experiments, an inflow velocity U = 0.183 m/s was employed, yielding a Reynolds number, Re = 1.2×10^4 based on model height. The bus model is shown schematically in Fig. 1. The length, height and width of the model were L = 175 mm, H = 66 mm and W = 56 mm, respectively. The model used in this work was intended to represent a medium sized bus. The model was one-fortieth of the bus which was under considerations, which assuming a typical travelling speed of 90 km/h, gives a prototype Re = 4.4×10^6. This is significantly different from the prototype conditions, one consequence of which is that the characteristics of wake region for a rounded afterbody are sensitive to the Reynolds number [10,13–16]. Despite this difference, we contend that the current work is complementary to CFD simulations and wind tunnel experiments for understanding the general wake flow phenomenon. For the present experiments the bus model was mounted on a 2 m long ground board in the test section of the water channel to simulate ground effects. The ground board spans the cross section of the tunnel and has a rounded leading edge to avoid flow separation. There are numerous methods

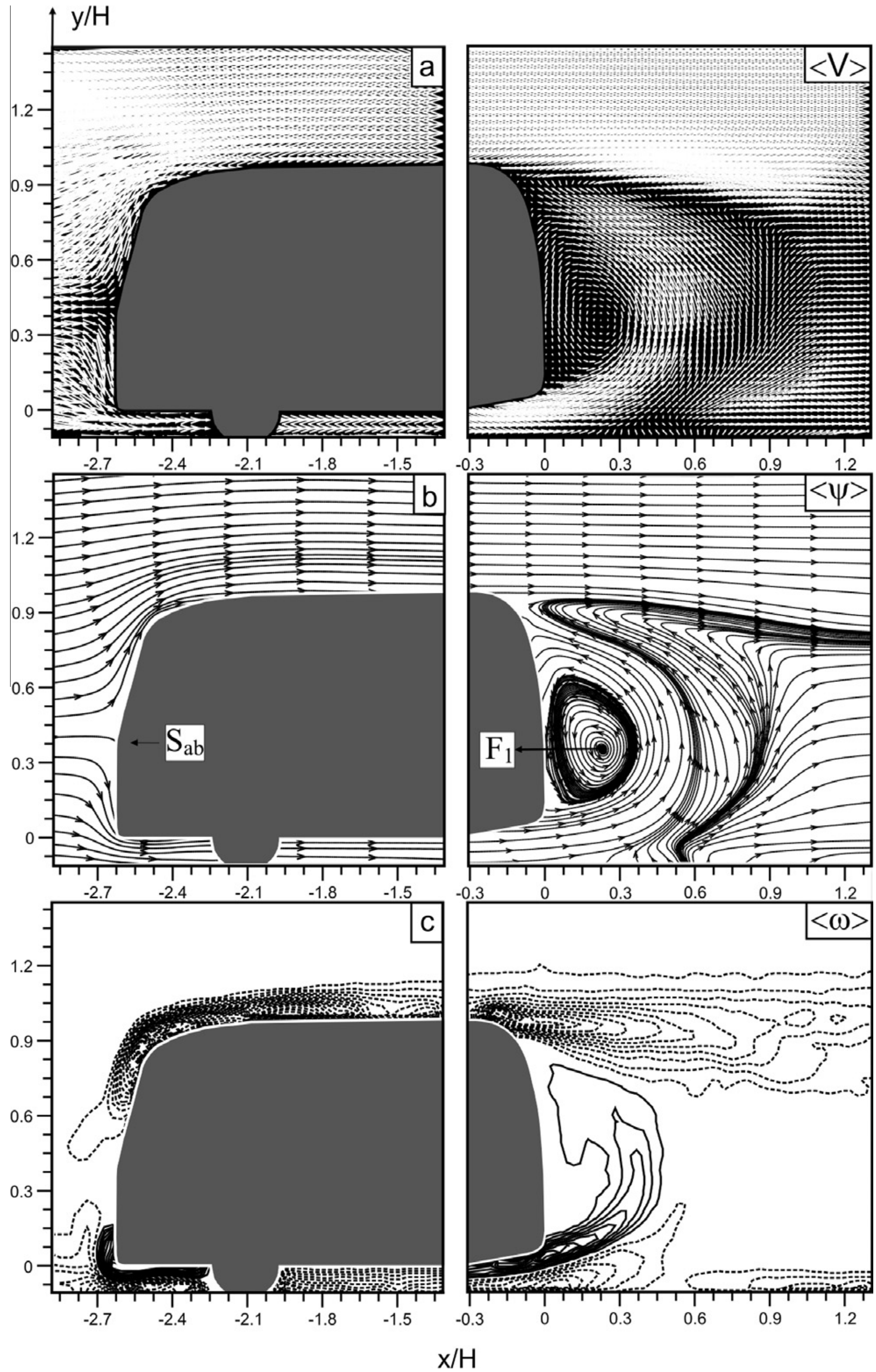

Fig. 5. Patterns of time-averaged velocity vector maps $\langle V\rangle$, streamlines $\langle\psi\rangle$ and vorticity contours $\langle\omega\rangle$ in the vertical symmetry plane $z = 0$. Minimum and incremental values of vorticity are $\langle\omega_{min}\rangle = \pm 2\ s^{-1}$ and $\Delta\langle\omega\rangle = 2\ s^{-1}$.

for simulating the real road conditions where vehicles move relative to the stationary road. The moving belt and a stationary elevated ground plane are the most widely used real road simulation techniques in numerical and experimental studies. Studies of road effects on the flow around ground vehicles showed that a moving ground has insignificant effects on the vehicle wake flow [17–19]. Our experimental set-up with an elevated stationary ground board is adopted as the simplest way to represent the road by some other authors [20–23]. Fig. 2 shows the location of the model in the water channel. The measurements were carried out in vertical, horizontal and cross-sectional planes (Fig. 3). The velocity fields were measured by Dantec PIV system which consisted of a dual-head Nd:YAG laser, a high resolution CCD camera, a synchronizer and optics. The Nd:YAG laser provided a maximum output energy of 120 mJ per pulse. The CCD camera had a spatial resolution of 1024×1024 pixels with a maximum frame rate of 15 frames per second and

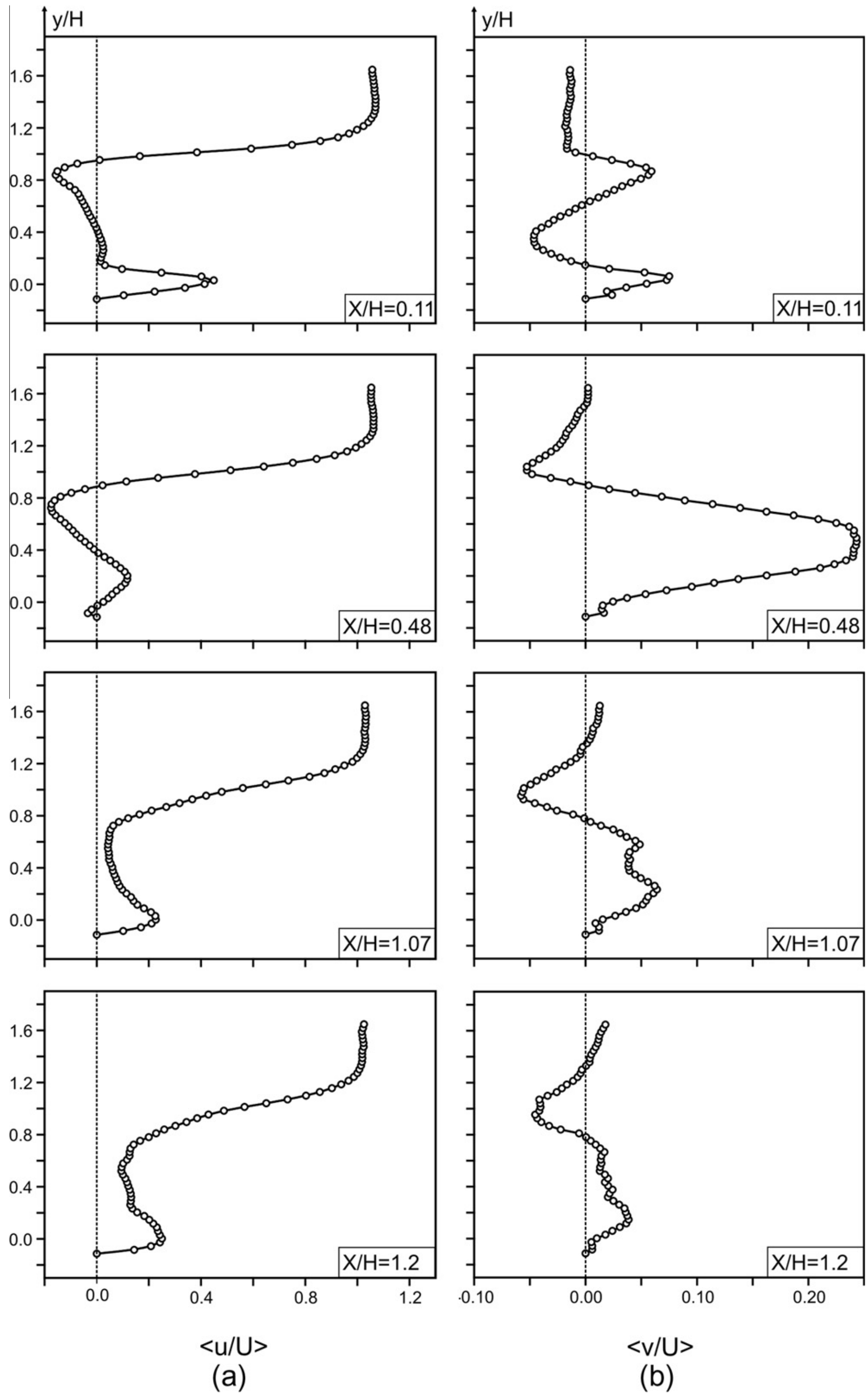

Fig. 6. Velocity profiles of the flow in the vertical symmetry plane $z = 0$ in the wake region. (a) Dimensionless streamwise velocity component $\langle u/U \rangle$. (b) Dimensionless spanwise velocity component $\langle v/U \rangle$.

equipped with a lens of a focal length of 60 mm. The Nd:YAG laser and CCD camera were synchronized using a Dantec Flow Map Processor. The flow was seeded with silver-coated spherical particles of 12 μm in diameter. The measuring plane was illuminated by a laser sheet generated from the Nd:YAG laser system. The time interval between pulses was 1.2 ms. The thickness of the laser sheet was approximately 2 mm. The time interval and the laser sheet thickness were selected such that the maximum amount of particle displacement in the interrogation window was obtained. Instantaneous velocity vector fields were generated using a cross-correlation technique between successive particle images. The raw velocity vector field was determined from this displacement vector field, using

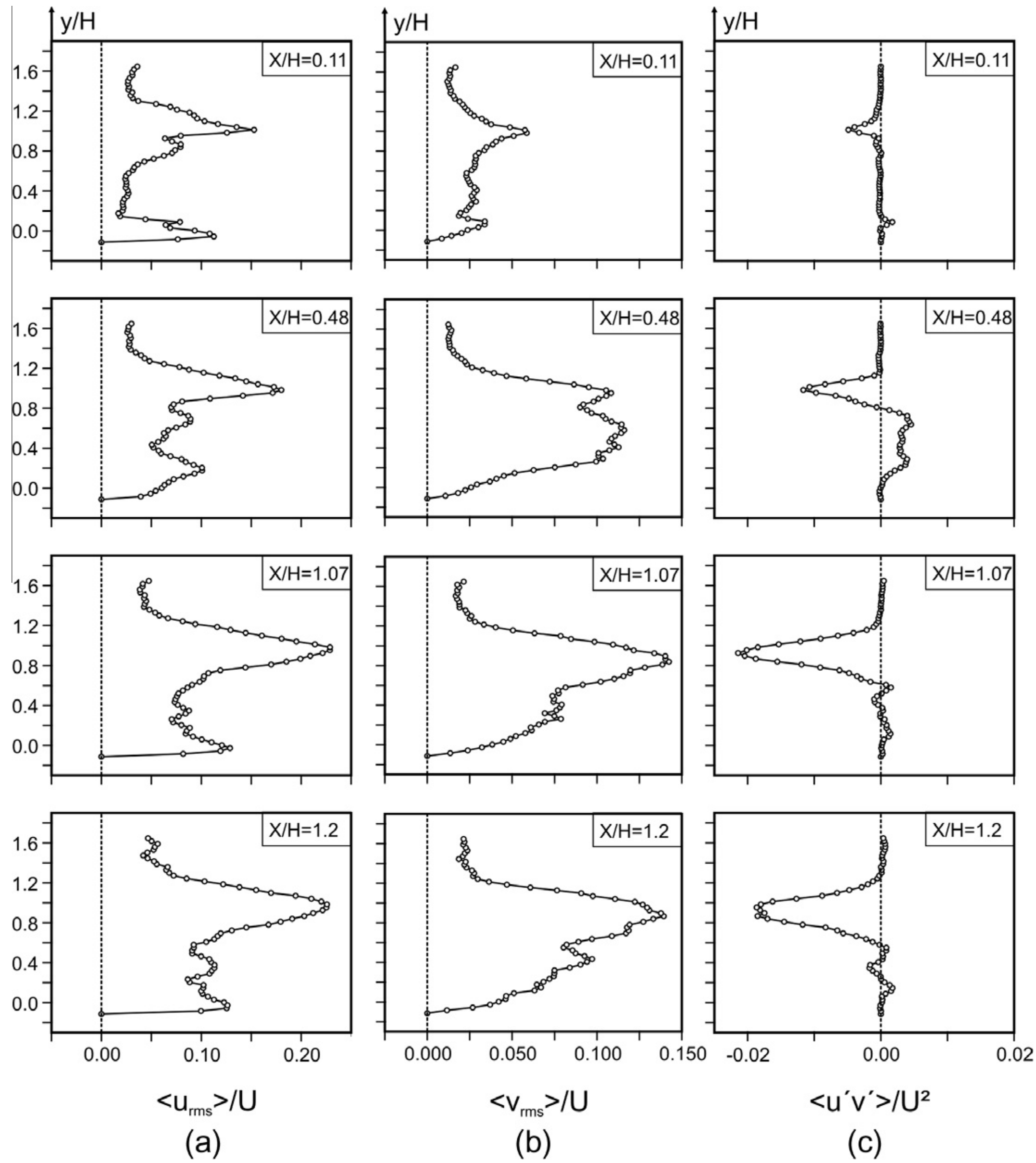

Fig. 7. Profiles of turbulence properties in the vertical symmetry plane $z = 0$ in the wake region. (a) Root mean square of streamwise velocity fluctuations $\langle u_{\mathrm{rms}}\rangle/U$. (b) Spanwise velocity fluctuations $\langle v_{\mathrm{rms}}\rangle/U$. (c) Reynolds stress correlations $\langle u'v'\rangle/U^2$.

the time interval between laser pulses. Spurious velocity vectors were then detected applying the local median-filter technique (Westerwell, [24]), and were replaced by interpolated vectors, calculated by means of a bilinear least-squares fit technique between neighboring vectors.

Uncertainty in velocity measurements is generally caused by the seeding particle size, non-uniform particle distribution, particle overlap, interrogation window size and electronic and optical image noise (Hart, [25]). In the current study, the number of particle images in an interrogation window was kept between 15 and 20, in order to satisfy the high-image-density criterion. The dimensions of the interrogation area employed throughout were 32 × 32 pixels with 50% overlap providing 3844 velocity vectors over the entire field of view plane. The PIV technique used in this study was similar to the one employed by Westerwell [26], who calculated that the uncertainty in the velocity field was less than 2%. Extensive information about these uncertainty factors affecting PIV measurements was reported by Hart, [25], Westerwell [26], Adrian [27], Gui et al. [28] and Adrian [29].

To determine the time-averaged mean flow structure, 300 instantaneous velocity fields were measured. Time-averaged parameters which are calculated from $N = 300$ PIV images, are calculated as follows:

Time-averaged streamwise component of velocity:

$$\langle u(x,y)\rangle = \frac{1}{N}\sum_{n=1}^{N} u_n(x,y)$$

Time-averaged transverse component of velocity:

$$\langle v(x,y)\rangle = \frac{1}{N}\sum_{n=1}^{N} v_n(x,y)$$

Time-averaged vorticity:

$$\langle \omega(x,y)\rangle = \frac{1}{N}\sum_{n=1}^{N}\omega_n(x,y)$$

Root-mean-square of u component fluctuation:

$$u_{rms} \equiv \langle u\rangle_{rms} \equiv \left[\frac{1}{N}\sum_{n=1}^{N}[u_n(x,y) - \langle u(x,y)\rangle]^2\right]^{1/2}$$

Root-mean-square of v component fluctuation:

$$v_{rms} \equiv \langle v\rangle_{rms} \equiv \left[\frac{1}{N}\sum_{n=1}^{N}[v_n(x,y) - \langle v(x,y)\rangle]^2\right]^{1/2}$$

Averaged value of Reynolds stress correlation:

$$\langle u'v'\rangle = \frac{1}{N}\sum_{n=1}^{N}[u_n(x,y) - \langle u(x,y)\rangle][v_n(x,y) - \langle v(x,y)\rangle]$$

The normalized boundary layer profile on the raised ground board in front of the bus model at $x/H = -3.3$ is plotted in Fig. 4. The flat plate 1/7th power law boundary layer profile is also given. The apparent agreement shows that the boundary layer on the ground board is turbulent.

3. Results and discussion

3.1. Time-averaged velocity field

Fig. 5 depicts the time-averaged velocity vector maps $\langle V\rangle$, the patterns of streamlines $\langle \psi\rangle$ and the corresponding vorticity contours $\langle \omega\rangle$ around the model in the vertical symmetry plane $z = 0$. The minimum and incremental values of the vorticity contours are $\langle \omega_{\min}\rangle = \pm 2\ \text{s}^{-1}$ and $\langle \Delta\omega\rangle = 2\ \text{s}^{-1}$, respectively. Contours of positive (counterclockwise) and negative (clockwise) vorticity are indicated by solid and dashed lines, respectively. Fig. 5 provides a clear view of flow structures near the front face, on the roof and in the wake region of the model. The approaching flow on the upstream of the model decelerates longitudinally and accelerates vertically to pass around the model. The streamlined flow is divided into upward and downward flows from the stagnation point, S_{ab} at the forward face of the model. Attached flow can be clearly seen on the leading part of the model roof due to the adequate rounded leading edge of the model. The attached flow moves further downstream along the roof surface and is separated at the trailing roof edge of the model. At the rear of the model a large reverse flow region is formed. The length of this recirculation region is approximately 0.92 times the height of the model. Foci F_1 located at a location of $x/H = 0.23$, $y/H = 0.37$ is clearly visible. Where H is the height of the bus model. Fig. 5c displays the upperbody and underbody wall shear layers. The upperbody has negative vorticity while the underbody shear layer has positive and negative vortices. The wake pattern is markedly asymmetric. The upper negative vortex moves almost along the horizontal direction while the positive lower vortex tends to move towards the top corner of the model. In conclusion, flow topologies reveal a well-defined circulating flow which occupies the wake flow region downstream of the model.

Fig. 6 shows the time-averaged normalized velocity profiles in the wake region downstream of the model at the selected locations on the vertical symmetry plane. Here, velocity components are normalized with the free-stream velocity, U. Fig. 6a shows the streamwise velocity profiles, $\langle u\rangle/U$ at different downstream locations behind the model. The negative velocity fields in between $x/H = 0.11$ and $x/H = 1.07$ represent the existence of the wake flow region downstream of the model. The maximum reversed velocity in the circulatory flow region is approximately 0.18 times the

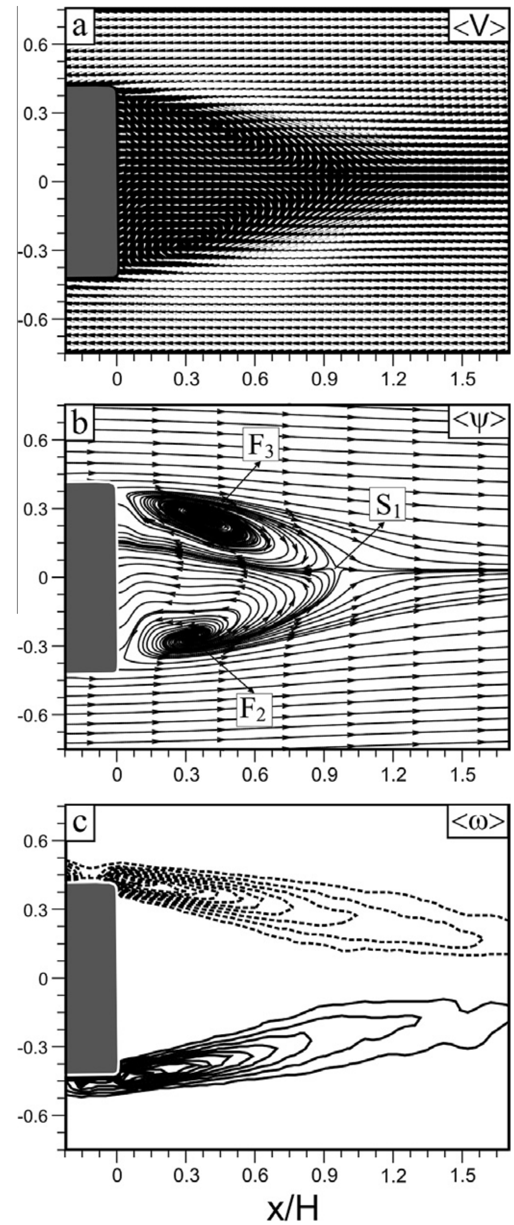

Fig. 8. Patterns of time averaged velocity vector maps $\langle V\rangle$, streamlines $\langle \psi\rangle$ and vorticity contours $\langle \omega\rangle$ in the horizontal xz-plane for $y/H = 0.5$. Minimum and incremental values of vorticity are $\langle \omega_{\min}\rangle = \pm 2\ \text{s}^{-1}$ and $\Delta\langle \omega\rangle = 2\ \text{s}^{-1}$.

freestream velocity, U at $y/H = 0.72$. At the first measuring section $x/H = 0.11$ the streamwise velocity, $\langle u\rangle/U$ takes positive values in the lower part of the velocity profile because of the jet flow occurring between the ground and the bottom surface of the model and streamwise velocity component increases in this region. The maximum positive velocity in this region is approximately 0.45 times the free-stream velocity, U at $y/H = 0.03$. The rate of increase in the streamwise velocity across the positive shear layer at the upper part of the model is due to the entrainment of wake and the core flow regions. In the middle part of the velocity profile there is a negative velocity field in between $y/H = 0.43$ and $y/H = 0.92$ which represents the reverse flow downstream of the model. The maximum negative velocity is approximately 0.15 times the free-stream velocity, U. At the second measuring section, $x/H = 0.48$ significant reverse flow in the downstream region of the model can be clearly seen between $y/H = 0.4$ and $y/H = 0.86$. The maximum reverse velocity in this measuring section is located at

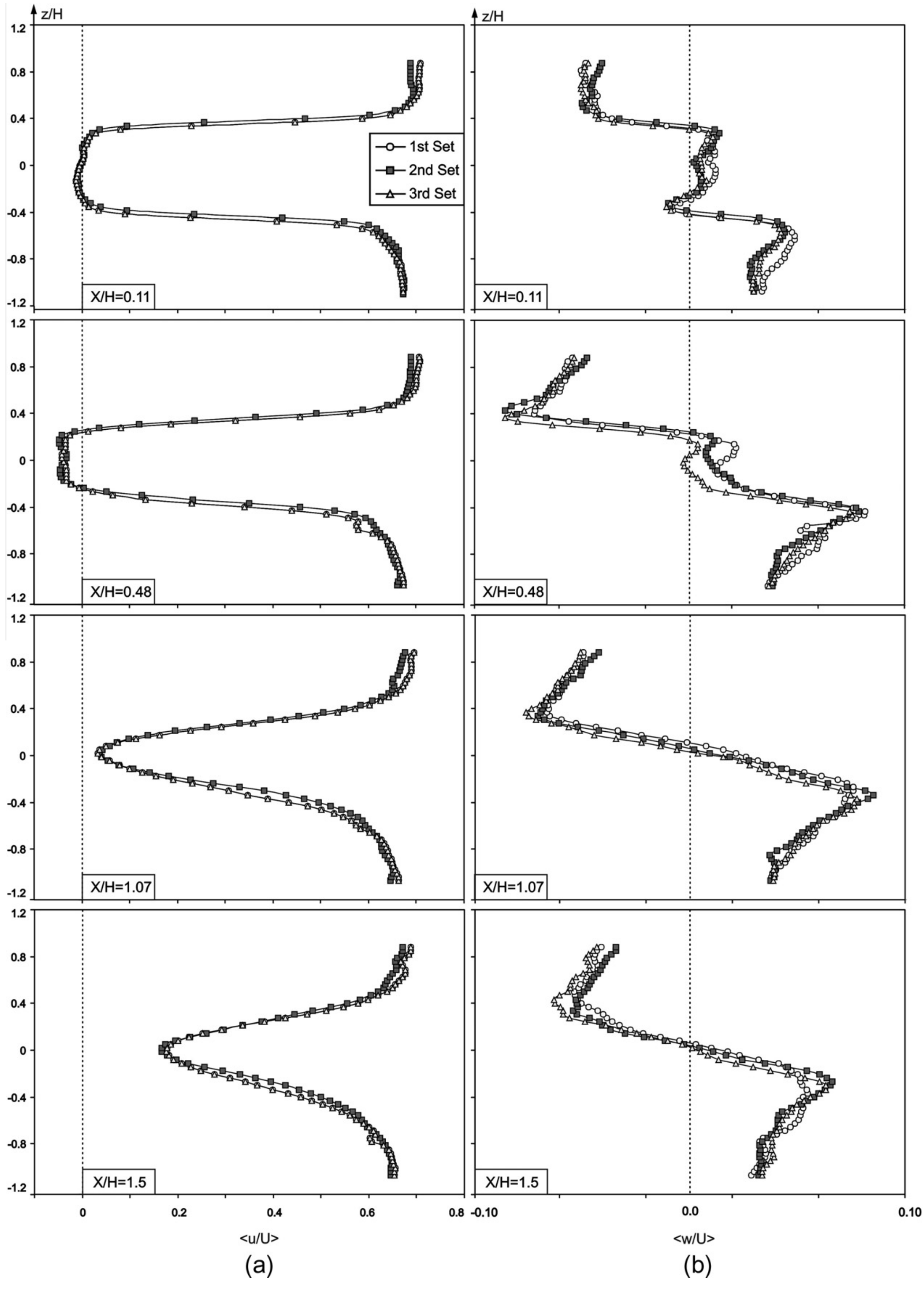

Fig. 9. Velocity profiles of the flow in the horizontal xz-plane for $y/H = 0.5$ in the wake region. (a) Dimensionless streamwise velocity component $\langle u/U \rangle$. (b) Dimensionless cross-stream velocity component $\langle w/U \rangle$.

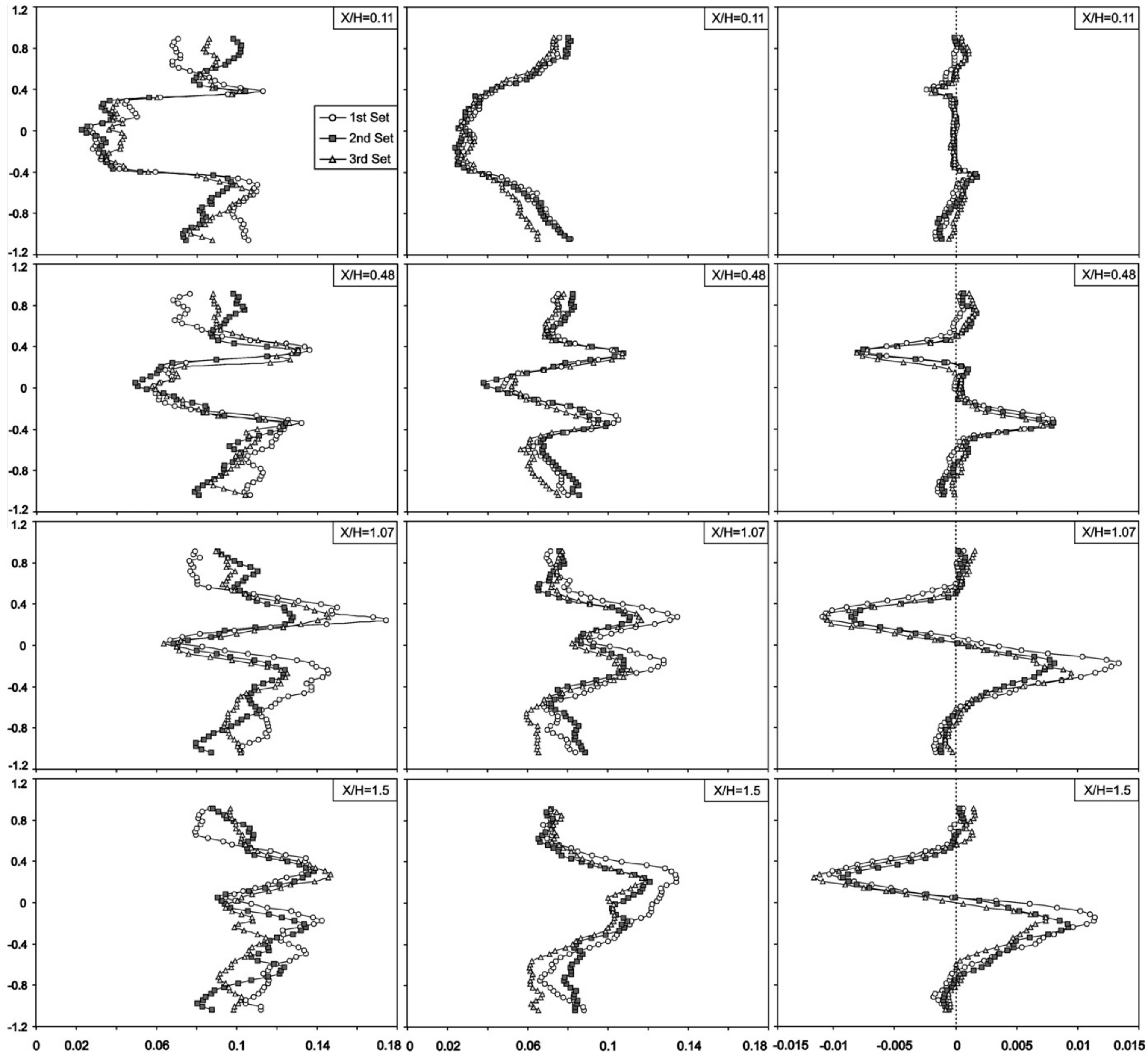

Fig. 10. Profiles of turbulence properties in the horizontal *xz*-plane for $y/H = 0.5$ in the wake region. (a) Root mean square of streamwise velocity fluctuations $\langle u_{rms}\rangle/U$. (b) Cross-stream velocity fluctuations $\langle w_{rms}\rangle/U$. (c) Reynolds stress correlations $\langle u'w'\rangle/U^2$.

$y/H = 0.72$ and approximately 0.18 times the free-stream velocity, U. Positive streamwise velocity values are identified in the third and fourth measuring sections $x/H = 1.07$ and $x/H = 1.5$, respectively.

Fig. 7 presents the profiles of the root mean square of streamwise and spanwise velocity components, $\langle u_{rms}\rangle/U$ and $\langle v_{rms}\rangle/U$ normalized by the free-stream velocity, U and Reynolds stress correlation, $\langle u'v'\rangle/U^2$ normalized by the square of the free-stream velocity in the central region of vertical plane. The peak values of turbulent properties take place along the upper-body and underbody shear layers. The magnitude of the root mean square of streamwise velocity fluctuations, $\langle u_{rms}\rangle/U$ shown in Fig. 7a are higher in the upper-body shear layer than in the underbody shear layer due to the high rate of momentum. The peak value of $\langle u_{rms}\rangle/U$ is approximately 0.23. The root mean square of spanwise velocity components, $\langle v_{rms}\rangle/U$ presented in Fig. 7b shows a similar trend. The maximum value of $\langle v_{rms}\rangle/U$ is approximately 0.14 which is smaller than the corresponding value of $\langle u_{rms}\rangle/U$ at the same location. Profiles of the Reynolds stress correlation, $\langle u'v'\rangle/U^2$ are shown in Fig. 7c. The maximum value of Reynolds stress correlation, $\langle u'v'\rangle/U^2$ appears along the upper-body shear layer with a magnitude of 0.02. Magnitude of Reynolds stress correlations, $\langle u'v'\rangle/U^2$ along the underbody shear layer are smaller comparing to the upper-body shear layer due to the ground effect.

Fig. 8 presents the time-averaged velocity vector maps $\langle V\rangle$, the patterns of streamlines $\langle\psi\rangle$ and the corresponding vorticity contours $\langle\omega\rangle$ downstream of the model in the horizontal *xz*-plane at an elevation of $y/H = 0.5$ at the geometrical center of the model. The minimum and incremental values of the vorticity contours are $\langle\omega_{min}\rangle = \pm 2\ s^{-1}$ and $\langle\Delta\omega\rangle = 2\ s^{-1}$, respectively. In the wake region downstream of the model the mean flow is almost symmetric with respect to the geometrical symmetry plane and a pair of recirculating region with similar size is identified. A pair of identical foci F_2 and F_3 at $x/H = 0.35$, $z/H = \pm 0.24$ and a saddle point S_1 at $x/H = 0.95$ are developed in the wake region. The saddle point, S_1 shown in Fig. 8b indicates the merging of shear layers emanating both sides of the bus model. Regions of negative and positive

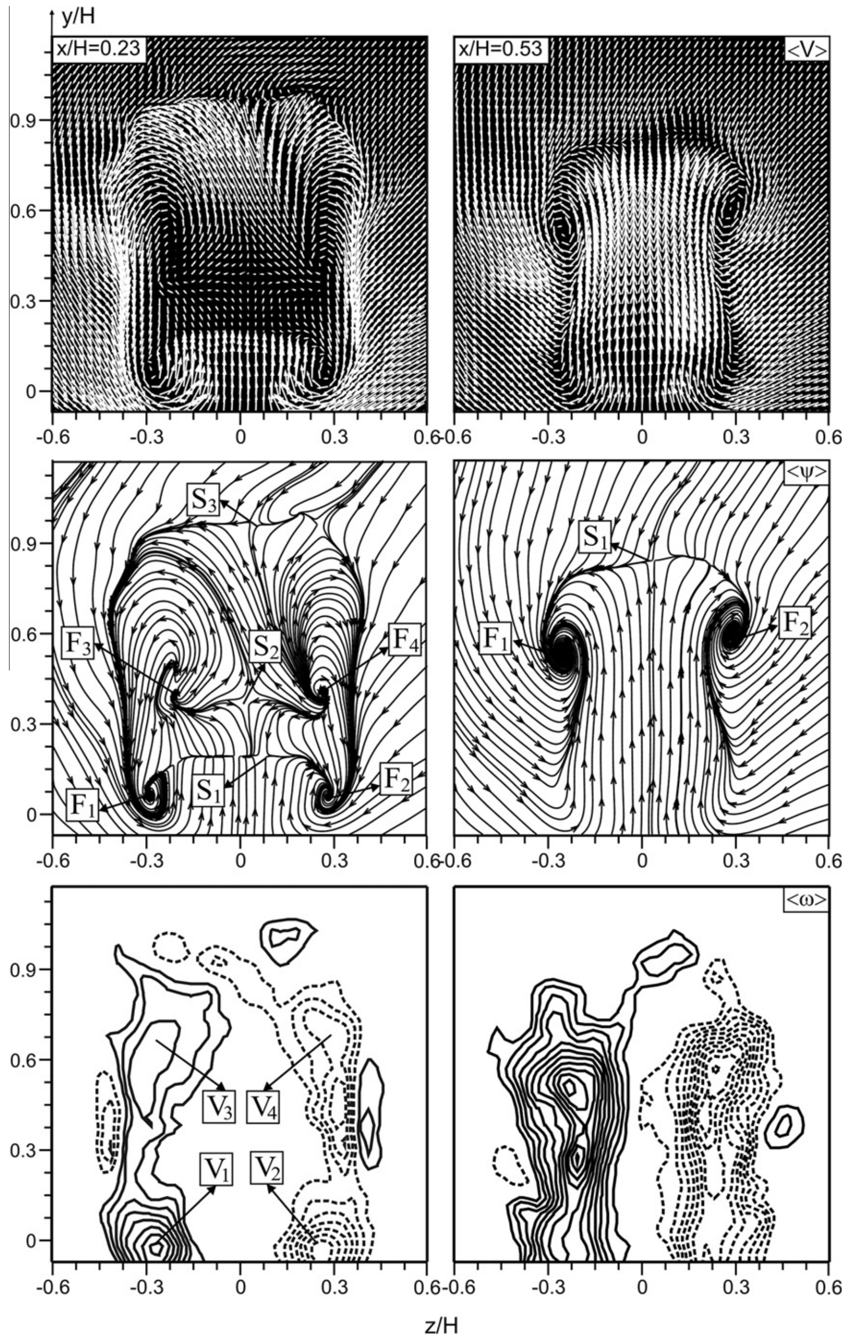

Fig. 11. Patterns of time averaged velocity vector maps $\langle V \rangle$, streamlines $\langle \psi \rangle$ and vorticity contours $\langle \omega \rangle$ in the cross-planes for $x/H = 0.23$ and $x/H = 0.53$. Minimum and incremental values of vorticity are $\langle \omega_{min} \rangle = \pm 0.5\ s^{-1}$ and $\Delta\langle \omega \rangle = 0.5\ s^{-1}$.

vorticity contours in Fig. 8c define the side wall shear layers. These two shear layers extend approximately up to the same downstream locations in the flow direction.

Fig. 9 presents the time-averaged velocity profiles on the horizontal *xz*-plane at an elevation of $y/H = 0.5$ in the wake region downstream of the model. Here three sets of data were measured at different period of time in order to see if there was a high level of discrepancy between these data sets. The total numbers of data was 350 for these three sets of data. The streamwise velocity profiles, $\langle u/U \rangle$ are shown in Fig. 9a. The reverse flow region occurs resulting in a negative streamwise velocity, u beginning from the rear surface of the model up to a point with a distance of $x/H = 1.07$. The flow characteristics are almost symmetric about the centerline of the model. Dimensionless cross-stream velocity component $\langle w/U \rangle$ shown in Fig. 9b shows that the maximum value of $\langle w/U \rangle$ occurs at $x/H = 1.07$ indicating that the maximum mixing fluids happen around this location. At the first station, $x/H = 0.11$, the magnitude of dimensionless cross-stream velocity components, $\langle w/U \rangle$ are smallest, but increases gradually until $x/H = 1.07$. Starting from this station, the level of the dimensionless cross-stream velocity component, $\langle w/U \rangle$ decays down gradually. The distance between maximum values of dimensionless cross-stream velocity components, $\langle w/U \rangle$ is maximum at $x/H = 0.11$, but this distance is minimum at $x/H = 1.5$. Comparisons of three sets of data indicate that there is a variation around 30% in the time-averaged spanwise velocity components, $\langle v/U \rangle$ in the horizontal plane at $X/H = 0.48$ for small area. In most points, there is a good agreement between three test sets of $\langle w/U \rangle$ along Z/H axes at all locations of X/H. Dimensionless velocity

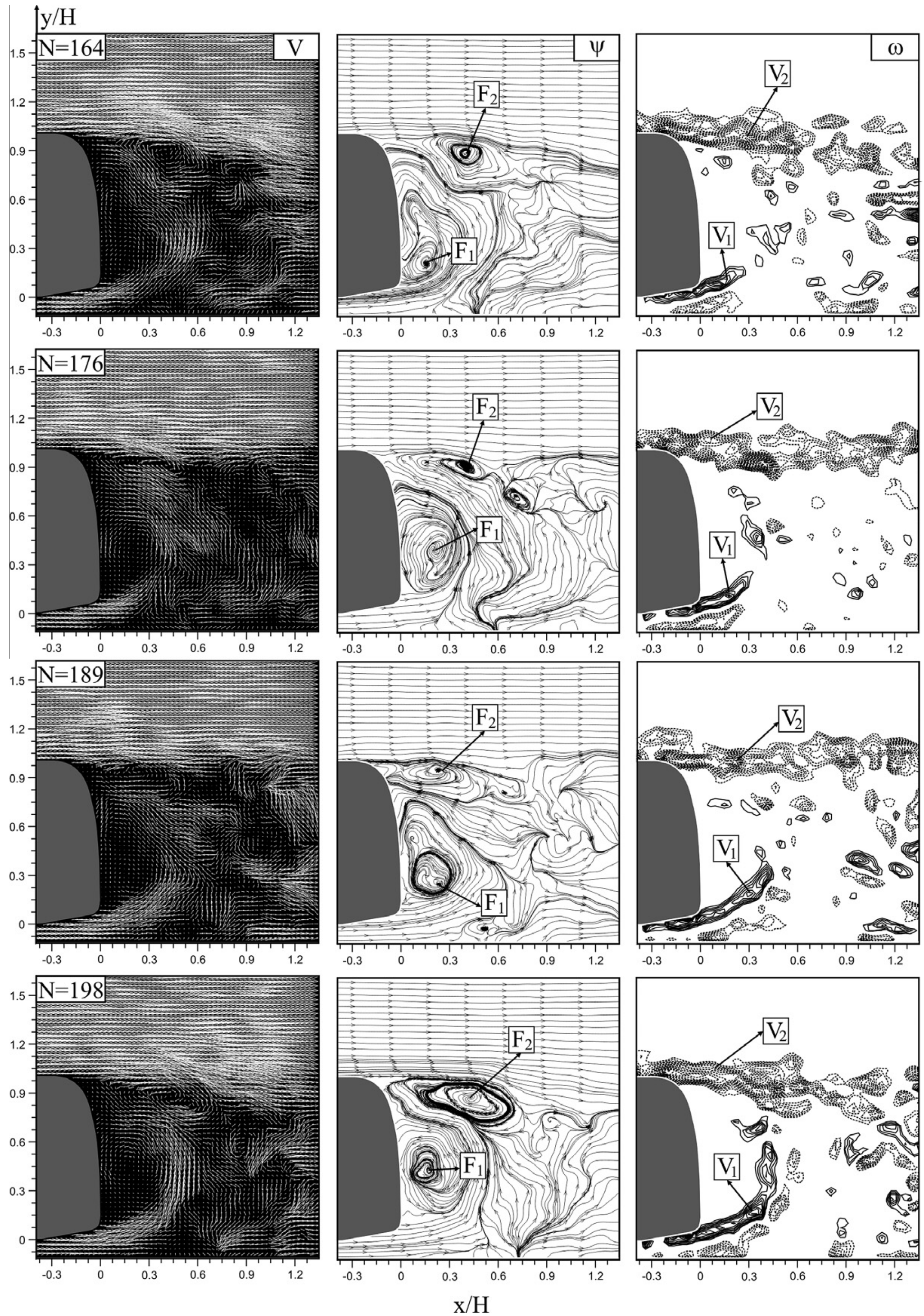

Fig. 12. Patterns of instantaneous velocity vectors V, streamlines ψ and vorticity contours ω, in the vertical symmetry plane $z = 0$ in the wake region. Minimum and incremental values of vorticity are $\omega_{min} = \pm 2\ s^{-1}$ and $\Delta\omega = 2\ s^{-1}$.

components $\langle u/U \rangle$ and $\langle w/U \rangle$ show that minimum velocity occurs at the central axis of measuring planes.

Fig. 10 shows profiles of three sets of the root mean square of streamwise and cross-stream velocity components, $\langle u_{rms}/U \rangle$,

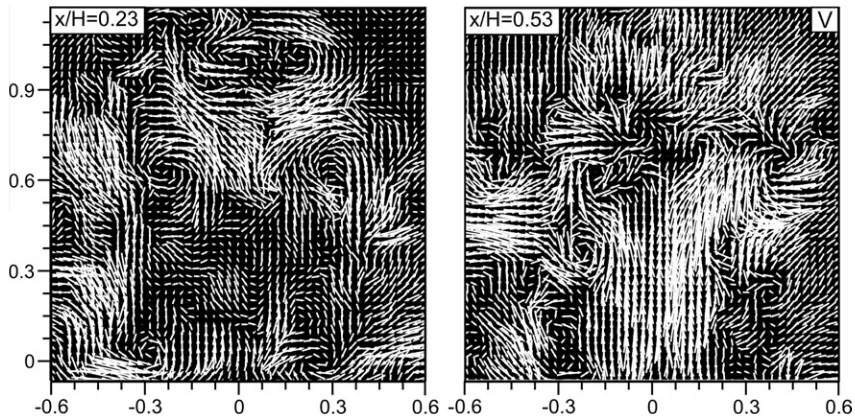

Fig. 13. Instantaneous velocity field in two cross-planes $x/H = 0.23$ and $x/H = 0.53$.

$\langle w_{rms}/U \rangle$ and the corresponding Reynolds stress correlations, $\langle u'w'/U^2 \rangle$ in the central region of the horizontal plane. The distributions of the root mean square of streamwise velocity fluctuations, $\langle u_{rms}/U \rangle$ shown in Fig. 10a indicate mainly two maxima at two different locations along the lateral directions which correspond to the edge shear layers. Although all sets of data follow the same trend, but there is a high rate of discrepancy between data sets. The fluctuations of the cross-stream velocity components $\langle w_{rms} \rangle/U$ in the lateral direction shown in Fig. 10b reveal that the values of $\langle w_{rms} \rangle/U$ are maximum on the shear layers. Circulatory flow motions which increase the rate of entrainment between the wake and the main flow regions take place along the both shear layers resulting in a high rate of fluctuations. Disagreements between three different test sets of $\langle w_{rms} \rangle/U$ are less comparing to the cases of $\langle u_{rms}/U \rangle$. Downstream of shear layers merging points, there is a high rate of velocity fluctuations which cause a high rate of disagreement between data set taken at different period of time at $X/H = 1.07$ and 1.5. Profiles of the Reynolds stress correlation, $\langle u'w' \rangle/U^2$ shown in Fig. 10c indicate that the peak values of the Reynolds stress correlations, $\langle u'w'/U^2 \rangle$ occur along the shear layers emerging from the both sides of the trailing edges of the bus model. Profiles of turbulence properties show that maximum fluctuations appear just downstream of the saddle point, S_1 at a location of $x/H = 1.07$ due to the high rate of mixing flows. Curves of the Reynolds stress correlations, $\langle u'w'/U^2 \rangle$ indicate that those three sets of data agree better comparing to the root mean square of streamwise and cross-stream velocity components, $\langle u_{rms}/U \rangle$, $\langle w_{rms}/U \rangle$, respectively. It can be concluded that one needs data more than 350 in order to have less disagreements between data set taken at different period of time when there is a high rate of velocity fluctuations. It should be stated that the present software program can only provide a total of 350 data.

Fig. 11 presents the time-averaged velocity vector maps $\langle V \rangle$, the patterns of streamlines $\langle \psi \rangle$ and the corresponding vorticity contours $\langle \omega \rangle$ in two *zy* cross-sections of end-view planes at $x/H = 0.23$ and $x/H = 0.53$ locations. The flow field downstream of the model at the location $x/H = 0.23$ is dominated by a pair of counter rotating trailing vortices (V3 and V4) originated from the bottom corners of the model. Han [30] found these vortices near the lower lateral edges of the Ahmed body and concluded that they were formed due to the viscous interaction between the body and the ground-plane boundary layer. The left (V1, V3) and right (V2, V4) vortices rotate counterclockwise and clockwise, respectively. The upwash flow is clearly visible between the counter rotating vortices. Further downstream at the location $x/H = 0.53$ two counter rotating longitudinal vortices originated from the upper corners of the model can be clearly identified. They are stronger than the vortices originating from the bottom corners of the model at the location $x/H = 0.23$. There is a strong upwash flow between the counter rotating longitudinal vortices. It is known that the model experiences lift and the sense of rotation of the vortices is seen to be compatible with this [31].

3.2. Instantaneous velocity field

The instantaneous flow structure in the wake region downstream of the model on the vertical symmetry plane $z = 0$ is shown in Fig. 12. The instantaneous wake is different from the time-averaged flow field and comparisons of the instantaneous flow structures reveal that additional vortices are generated. Swirling patterns of velocity vectors take place along the upperbody shear layer. On the other hand, well-defined large-scale swirling patterns of velocity vectors are evident on the bottom edge. The positive vorticity layer separating from the lower edge of the model diverges substantially and, tends to interact with the cluster of vorticity of the separating layer emerging from the roof surface of the model. The negative vortex originating from the upperbody shear layer moves almost along the horizontal direction. The point of attachment on the ground surface travels forward and backward in the flow direction in an unsteady mode. Shear layers emanating from the upperbody and underbody surface create a complex flow field which consists of a number of vortices that move randomly in time and space. The intensity and domain of vortices, ω, emanating from the bottom trailing edge of the model is higher comparing to those vortices occur downstream of the model.

In conclusion, flow structures downstream of the model changes rapidly and in a random mode. The size of the wake region of this model is substantially smaller comparing to results of the rectangular bus model obtained by Gurlek et al. [7].

Fig. 13 depicts the instantaneous velocity fields in cross-planes. The instantaneous wake in the cross-plane is different from the time-averaged one and it was found that the mean trailing vortices form as a result of several instantaneous vortices. The instantaneous wake region was found to consist of a substantial number of coherent vortex structures that move randomly in time and space. Many longitudinal vortex structures observed in the instantaneous flow field will have originated from various features of the complex bus body.

4. Conclusion

Understanding the aerodynamic characteristics of passenger vehicles are important for reducing fuel consumption, improving fuel economy, vehicle performance and passenger comfort. The three-dimensional flow structures around a bus model have been investigated experimentally using digital particle image velocimetry (DPIV).

Attached flow can be clearly seen on the front part of the model roof due to the adequate rounded leading edge of the model in the vertical symmetry plane. In the wake flow region downstream of the model a large reverse flow region is formed. The length of this recirculation region is approximately 0.92 times the height of the model.

The wake pattern is markedly asymmetrical. The upper negative vortex moves almost along the horizontal direction while the positive lower vortex tends to move towards the top corner of the model.

In the horizontal plane a pair of recirculating flow region with a similar size is identified in the wake region. The length of the wake flow region is found to be approximately 0.95 times the height of the model. The maximum values of turbulence intensities are found along the upperbody and underbody shear layers in both vertical and horizontal measuring planes.

In cross-planes the flow field downstream of the model is dominated by a pair of counter rotating vortices originating from the bottom and upper corners of the model.

The instantaneous wake flow characteristics are different from the time-averaged flow data and contain not only two longitudinal vortices but a larger number of vortices that move randomly in time and space.

Acknowledgment

The authors would like to acknowledge the financial support of the Office of Scientific Research Projects of Cukurova University for funding under contract No: MMF2006D32.

References

[1] W.H. Hucho, Aerodynamics of Road Vehicles, SAE International Press, 1998.
[2] S.R. Ahmed, G. Ramm, G. Faltin, Some salient features of the time averaged ground vehicle wake, SAE Paper 840300, 1984.
[3] E.G. Duell, A.R. George, Experimental study of a ground vehicle body unsteady near wake, SAE Paper 1999-01-0812, 1999.
[4] A. Spohn, P. Gillieron, Flow separations generated by a simplified geometry of an automotive vehicle, in: IUTAM Symposium on Unsteady Separated Flows, 8–12 April, Toulouse, France, 2002.
[5] H. Lienhart, S. Becker, Flow and turbulente structure in the wake of a simplified car model, SAE Paper 2003-01-0656, 2003.
[6] G. Vino, S. Watkins, P. Mousley, J. Watmuff, S. Prasad, Flow structures in the near-wake of the Ahmed model, J. Fluids Struct. 20 (2005) 673–695.
[7] C. Gurlek, B. Sahin, C. Ozalp, H. Akilli, Flow structures around a three-dimensional rectangular body with ground effect, Wind Struct. Int. J. 11 (5) (2008) 345–359.
[8] J. Leuschen, K.R. Cooper, Summary of full-scale wind tunnel tests of aerodynamic drag-reducing devices for tractor-trailers, The Aerodynamics of Heavy Vehicles II: Trucks, Buses, and Trains, Springer, New York, 2009.
[9] S. Krajnovic, L. Davidson, Large-eddy simulation of the flow around a simplified bus, in: Third Afosr International Conference on DNS and LES, University of Texas at Arlington, Texas, USA, 2001.
[10] S. Krajnovic, L. Davidson, Numerical study of the flow around a bus-shaped body, ASME J. Fluids Eng. 125 (2003) 500–509.
[11] D.B. Sims-Williams, B.D. Duncan, The Ahmed model unsteady wake: experimental and computational analyses, SAE Paper 2003-01-1315, 2003.
[12] P.S. Bernard, P. Collins, M. Potts, Vortex method simulation of ground vehicle aerodynamics, SAE Paper 2005-01-0549, 2005.
[13] K.R. Cooper, The effect of front-edge rounding and rear edge shaping on the aerodynamic drag of bluff vehicles in ground proximity, SAE Paper 850288, 1985.
[14] G. Buresti, R. Fedeli, A. Ferraresi, Influence of afterbody rounding on the pressure drag of an axisymmetrical bluff body, J. Wind Eng. Ind. Aerod. 69–71 (1997) 179–188.
[15] S. Krajnovic, L. Davidson, Flow around a simplified car. Part 1: Large eddy simulation, ASME J. Fluids Eng. 127 (2005) 907–918.
[16] E. Wassen, S. Eichinger, F. Thiele, Simulation of active drag reduction for a square-back vehicle,in: Conference Active Flow Control II, 26–28 May, Berlin, Germany, 2010.
[17] J.E. Hackett, J.E. Williams, J.B. Baker, S.B. Wallis, On the influence of ground movement and wheel rotation in the test on modern car shapes, SAE Technical Paper 870245, 1987.
[18] P.W. Bearman, D. De Beer, E. Hamidy, J.K. Harvey, The effect of a moving floor on wind tunnel simulation of road vehicles, SAE Technical Paper 880245, 1989.
[19] S. Krajnovic, L. Davidson, Influence of floor motion in wind tunnels on the aerodynamics of road vehicles, J. Wind Eng. Ind. Aerod. 93 (9) (2005) 677–696.
[20] A.M. Al-Garni, L.P. Bernal, B. Khalighi, Experimental investigation of the flow around a generic SUV, SAE Paper 2004-01-0228, 2004.
[21] M. Gohlke, J.F. Beaudoin, M. Amielh, F. Anselmet, Experimental analysis of flow structures and forces on a 3D-bluff-body in constant cross-wind, Exp. Fluids 43 (2007) 579–594.
[22] T.L. Chan, K. Gosse, Y. Zhou, S.C. Lee, X.W. Wang, J.F. Huang, Effect of rear slant angle on flow structures, and pollutant dispersion and concentration fields in the wake of the studied model vehicle, Int. J. Heat Mass Transfer. 51 (2008) 6180–6193.
[23] J.F. Huang, T.L. Chan, Y. Zhou, Three-dimensional flow structure measurements behind a queue of studied model vehicles, Int. J. Heat Mass Transfer. 30 (2009) 647–657.
[24] J. Westerwell, Efficient detection of spurious vectors in particle image velocimetry data, Exp. Fluids 16 (1994) 236–247.
[25] D.P. Hart, PIV error correction, Exp. Fluids 29 (2000) 13–22.
[26] J. Westerwell, Digital Particle Image Velocimetry Theory and Application, Delft University Press, 1993.
[27] R.J. Adrian, Particle-imaging techniques for experimental fluid mechanics, Annu. Rev. Fluid Mech. 23 (1991) 261–304.
[28] L. Gui, W. Merzkirch, R. Fei, A digital mask technique for reducing the bias error of the correlation-based PIV interrogation algorithm, Exp. Fluids 29 (2000) 30–35.
[29] R.J. Adrian, Twenty years of particle image velocimetry, Exp. Fluids 39 (2005) 159–169.
[30] T. Han, Computational analysis of three-dimensional turbulent flow around a bluff body in ground proximity, AIAA J. 27 (9) (1989) 1213–1219.
[31] P.W. Bearman, Near wake flows behind two-dimensional and three-dimensional bluff bodies, J. Wind Eng. Ind. Aerodyn. 69–71 (1997) 33–54.